Astronomy & Astrophysics

Transition from anti-solar to solar-like differential rotation: Dependence on Prandtl number

P. J. Käpylä[1,2]

[1] Georg-August-Universität Göttingen, Institut für Astrophysik und Geophysik, Friedrich-Hund-Platz 1, 37077 Göttingen, Germany
e-mail: pkaepyl@uni-goettingen.de
[2] KTH Royal Institute of Technology and Stockholm University, Hannes Alfvéns väg 12, 10691 Stockholm, Sweden

ABSTRACT

Context. Late-type stars such as the Sun rotate differentially due to the interaction of turbulent convection and rotation.
Aims. The aim of the study is to investigate the effects of the effective thermal Prandtl number, which is the ratio of kinematic viscosity to thermal diffusivity, on the transition from anti-solar (slow equator, fast poles) to solar-like (fast equator, slow poles) differential rotation.
Methods. Three-dimensional hydrodynamic and magnetohydrodynamic simulations in semi-global spherical wedge geometry were used to model the convection zones of solar-like stars.
Results. The overall convective velocity amplitude increases as the Prandtl number decreases, in accordance with earlier studies. The transition from anti-solar to solar-like differential rotation is insensitive to the Prandtl number for Prandtl numbers below unity, but for Prandtl numbers greater than unity, solar-like differential rotation becomes significantly harder to excite. Magnetic fields and more turbulent regimes with higher fluid and magnetic Reynolds numbers help to achieve solar-like differential rotation in near-transition cases where anti-solar rotation is found in more laminar simulations. Solar-like differential rotation occurs only in cases with radially outward turbulent angular momentum transport due to the Reynolds stress at the equator. The dominant contribution to this outward transport near the equator is due to prograde propagating thermal Rossby waves.
Conclusions. The differential rotation is sensitive to the Prandtl number only for large Prandtl numbers in the parameter regime explored in this study. Magnetic fields have a greater effect on the differential rotation, although the inferred presence of a small-scale dynamo did not lead to drastically different results. The dominance of the thermal Rossby waves in the simulations is puzzling because they are not detected in the Sun. The current simulations are shown to be incompatible with the currently prevailing mean-field theory of differential rotation.

Key words. turbulence – convection – dynamo – Sun: rotation

1. Introduction

The interplay of turbulent convection with the overall rotation of the Sun is the primary cause of differential rotation that is observed at the solar surface and in the interior (e.g., Rüdiger 1989; Miesch & Toomre 2009). Three-dimensional numerical simulations solving the equations of magnetohydrodynamics (MHD) capture the essence of this process and routinely produce solutions that are qualitatively similar to those for the Sun with equatorial acceleration (e.g., Gilman 1983; Brun et al. 2004; Guerrero et al. 2013; Käpylä et al. 2014). However, it has become increasingly clear recently that even the most sophisticated current simulations are missing something essential. The most striking manifestation of this is that simulations using a nominal solar luminosity and rotation rate often produce anti-solar (AS) differential rotation with equatorial deceleration (e.g., Fan & Fang 2014; Käpylä et al. 2014; Hotta et al. 2015), whereas solar-like (SL) differential rotation is achieved only with significantly more rapid rotation (e.g., Viviani et al. 2018; Matilsky et al. 2020).

This is related to the convective conundrum (O'Mara et al. 2016), which is essentially the difference between large-scale velocity amplitudes in simulations in comparison to the Sun (e.g., Hanasoge et al. 2012, 2016; Schumacher & Sreenivasan 2020). Until recently, the most common way to ensure SL differential rotation in simulations with solar luminosity and rotation rate has been to lower the convective velocities by artificially enhancing the radiative diffusivity (e.g., Fan & Fang 2014; Käpylä et al. 2014; Hotta et al. 2016). This cannot be justified based on physical grounds, however, since convection is thought to carry practically all of the energy flux through the solar convection zone (CZ), with the exception of very deep layers. Another more plausible effect is due to magnetic fields: it is conceivable that sufficiently strong fields can suppress convection on large scales to a degree where the differential rotation flips from AS to SL. Early results with relatively low-resolution simulations were mixed: Karak et al. (2015) found essentially no dependence on the magnetic field, while Fan & Fang (2014) and Simitev et al. (2015) reported more positive outcomes. Nevertheless, the magnetic Reynolds numbers of these simulations were most probably not high enough to excite a small-scale dynamo. This was addressed by the recent high-resolution simulations of Hotta & Kusano (2021) and Hotta et al. (2022), which suggest that SL differential rotation can indeed be achieved with the help of an efficient small-scale dynamo.

Another important parameter is the Prandtl number, Pr = ν/χ, where ν is the kinematic viscosity and χ is the thermal diffusivity. The notion that the solar convection zone is

operating in a regime in which the effective Prandtl number is large has recently gained popularity (e.g., O'Mara et al. 2016; Bekki et al. 2017; Karak et al. 2018). While these studies indicate that the overall velocity amplitudes are decreased in these set-ups, the problem with the differential rotation is even exacerbated (Karak et al. 2018). This is because it is not only the velocity amplitude that is sensitive to Pr, but turbulent transport of angular momentum and heat are also affected (e.g., Cattaneo et al. 1991; Käpylä 2021). Furthermore, theoretical arguments suggest that Pr ≪ 1 in the solar CZ (e.g., Ossendrijver 2003; Schumacher & Sreenivasan 2020).

Prandtl numbers that strongly deviate from unity are challenging numerically, and therefore most simulations are conducted in the Pr ≈ 1 regime. It is commonly acknowledged that reaching realistic parameter regimes in terms of, for example, Prandtl, Reynolds, and Rayleigh numbers with current or foreseeable simulations of stellar convection is not feasible (e.g., Kupka & Muthsam 2017). The main aim of the present study is to vary the Prandtl number within the range that can be achieved with numerical simulations with values above and below unity. The current study is also inspired by recent results from hydrodynamic non-rotating convection in Cartesian geometry (Käpylä 2021), where the convective energy transport and velocity statistics were found to be sensitive to the effective Prandtl number.

2. The model

The simulation set-up is similar to the set-ups used in Käpylä et al. (2019) and Käpylä et al. (2020). The simulation domain is a spherical wedge that spans $r_{\rm in} < r < R$ in radius, where $r_{\rm in} = 0.7R$ and R is the radius of the star, $\theta_0 < \theta < \pi - \theta_0$ in colatitude, where $\theta_0 = \pi/12$, and $0 < \phi < \pi/2$ in longitude. Equations of fully compressible MHD were solved,

$$\frac{\partial \boldsymbol{A}}{\partial t} = \boldsymbol{U} \times \boldsymbol{B} - \eta\mu_0 \boldsymbol{J}, \tag{1}$$

$$\frac{D\ln\rho}{Dt} = -\boldsymbol{\nabla}\cdot\boldsymbol{U}, \tag{2}$$

$$\frac{D\boldsymbol{U}}{Dt} = \boldsymbol{g} - 2\boldsymbol{\Omega}_0 \times \boldsymbol{U} - \frac{1}{\rho}(\boldsymbol{\nabla}p - \boldsymbol{J}\times\boldsymbol{B} - \boldsymbol{\nabla}\cdot 2\nu\rho\mathsf{S}), \tag{3}$$

$$T\frac{Ds}{Dt} = \frac{1}{\rho}\left[\eta\mu_0\boldsymbol{J}^2 - \boldsymbol{\nabla}\cdot(\boldsymbol{F}^{\rm rad} + \boldsymbol{F}^{\rm SGS})\right] + 2\nu\mathsf{S}^2, \tag{4}$$

where $\boldsymbol{A}$ is the magnetic vector potential, $\boldsymbol{U}$ is the velocity, $\boldsymbol{B} = \boldsymbol{\nabla}\times\boldsymbol{A}$ is the magnetic field, η is the magnetic diffusivity, μ_0 is the permeability of vacuum, $\boldsymbol{J} = \boldsymbol{\nabla}\times\boldsymbol{B}/\mu_0$ is the current density, $D/Dt = \partial/\partial t + \boldsymbol{U}\cdot\boldsymbol{\nabla}$ is the advective time derivative, ρ is the density, and $\boldsymbol{g} = -\boldsymbol{\nabla}\phi$ is the acceleration due to gravity, where $\phi = -GM/r$ is a fixed spherically symmetric gravitational potential, with G and M being the universal gravitational constant and the stellar mass, respectively. $\boldsymbol{\Omega}_0 = (\cos\theta, -\sin\theta, 0)\Omega_0$ is the angular velocity vector, where Ω_0 is the rotation rate of the frame of reference, p is the pressure, ν is the kinematic viscosity, T is the temperature, and s is the specific entropy with $Ds = c_{\rm V}D\ln p - c_{\rm P}D\ln\rho$, where $c_{\rm V}$ and $c_{\rm P}$ are the specific heat capacities in constant volume and pressure, respectively. The gas is assumed to obey the ideal gas law, $p = \mathcal{R}\rho T$, where $\mathcal{R} = c_{\rm P} - c_{\rm V}$ is the gas constant. The rate of strain tensor is given by

$$\mathsf{S}_{ij} = \frac{1}{2}(U_{i;j} + U_{j;i}) - \frac{1}{3}\delta_{ij}\boldsymbol{\nabla}\cdot\boldsymbol{U}, \tag{5}$$

where the semicolons refer to covariant derivatives (Mitra et al. 2009). The radiative flux is given by

$$\boldsymbol{F}^{\rm rad} = -K\boldsymbol{\nabla}T, \tag{6}$$

where K is the heat conductivity. The latter consists of two parts, $K = K_1 + K_2$, where $K_1 = K_1(r)$ is a fixed function of height and $K_2 = K_2(\rho, T)$ is density- and temperature-dependent according to Kramers opacity law (Weiss et al. 2004). The profile of K_1 is given by

$$K_1 = K_{\rm top}\left[1 + \tanh\left(\frac{r-R}{d_K}\right)\right], \tag{7}$$

where $K_{\rm top} = 2c_{\rm P}F_{\rm bot}/|g(R)|$, with $F_{\rm bot} = L/4\pi r_{\rm in}^2$ where L is the luminosity of the star, and where $d_K = 0.015R$. The contribution K_2 is given by

$$K_2(\rho, T) = K_0(\rho/\rho_0)^{-(a+1)}(T/T_0)^{3-b}, \tag{8}$$

where ρ_0 and T_0 are reference values of density and temperature, and the values $a = 1$ and $b = -7/2$ correspond to the Kramers opacity law. This formulation was first used in convection simulations by Brandenburg et al. (2000).

The subgrid scale (SGS) flux is given by

$$\boldsymbol{F}^{\rm SGS} = -\chi_{\rm SGS}\rho\boldsymbol{\nabla}s', \tag{9}$$

where $\chi_{\rm SGS}$ is the (constant) SGS diffusion coefficient for the entropy fluctuation $s'(r, \theta, \phi) = s - \langle s\rangle_{\theta\phi}$, where $\langle s\rangle_{\theta\phi}$ is the spherically symmetric part of the specific entropy. The SGS flux does not contribute to the net radial energy transport because it is decoupled from the mean stratification, and therefore changing $\chi_{\rm SGS}$ does not lead to drastic changes in the boundary layer thickness near the surface.

The simulations were made using the PENCIL CODE[1] (Brandenburg 2021). The code in this study employs third-order temporal and sixth-order spatial discretisation. Advective terms in Eqs. (1)–(4) are written as fifth-order upwinding derivatives with a sixth-order hyperdiffusive correction, where the diffusion coefficient is flow-dependent; see Appendix B of Dobler et al. (2006).

2.1. System parameters and diagnostics quantities

The simulations are defined by the energy flux imposed at the bottom boundary, $F_{\rm bot} = -(K\partial T/\partial r)|_{r=r_{\rm in}}$, the values of K_0, a, b, ρ_0, T_0, Ω_0, ν, η, $\chi_{\rm SGS}$, the profile of K_1, and the value of the modified Stefan-Boltzmann constant $\sigma_{\rm SB}$ in the upper boundary condition $\sigma_{\rm SB}T_{\rm surf}^4 = -K\partial T/\partial r$, where $T_{\rm surf}$ is the (unconstrained) surface temperature. The current models use a significantly enhanced luminosity in comparison to real stars to bring the thermal and dynamical timescales close enough to be resolved in the simulations. This leads to correspondingly higher convective velocities, and therefore, the rotation rate is increased accordingly to capture a similar rotational influence on the flow in the simulations in comparison to real stars; see Appendix A of Käpylä et al. (2020).

The non-dimensional luminosity is given by

$$\mathcal{L} = \frac{L_0}{\rho_0(GM)^{3/2}R^{1/2}}, \tag{10}$$

where ρ_0 is the initial density at the base of the convection zone. The degree of luminosity enhancement is given by the ratio $L_{\rm ratio} = \mathcal{L}/\mathcal{L}_\odot \approx 2.1 \times 10^5$, where $\mathcal{L}_\odot$ is the dimensionless solar luminosity. The initial stratification is determined by the non-dimensional pressure scale height at the surface,

$$\xi_0 = \frac{\mathcal{R}T_1}{GM/R}, \tag{11}$$

where $T_1 = T(R, t = 0)$.

---

[1] https://github.com/pencil-code/

The relative strengths of viscosity, SGS diffusion, and magnetic diffusivity are given by the SGS and magnetic Prandtl numbers,

$$\mathrm{Pr_{SGS}} = \frac{\nu}{\chi_{\mathrm{SGS}}}, \quad \mathrm{Pm} = \frac{\nu}{\eta}. \qquad (12)$$

We use $\mathrm{Pm} = 1$ in most of the runs and vary $\mathrm{Pr_{SGS}}$ between 0.1 and 10. The thermal Prandtl number related to the radiative conductivity is given by

$$\mathrm{Pr} = \frac{\nu}{\chi}, \qquad (13)$$

where $\chi = K/c_{\mathrm{P}}\rho$ is the radiative diffusivity, which in general varies as a function of radius, latitude, and time. In the current simulations, $\chi_{\mathrm{SGS}} \gg \chi$ almost everywhere. The efficiency of convection is quantified by the Rayleigh number,

$$\mathrm{Ra} = \frac{GM(\Delta r)^4}{\nu \chi_{\mathrm{s}} R^2} \left(-\frac{1}{c_{\mathrm{P}}} \frac{\mathrm{d}s_{\mathrm{hs}}}{\mathrm{d}r} \right)_{r_{\mathrm{s}}}, \qquad (14)$$

where $\Delta r = 0.3R$ is the depth of the layer, s_{hs} is the specific entropy in a one-dimensional non-convecting hydrostatic model, evaluated near the top of the domain at $r_{\mathrm{s}} = 0.95R$, and where χ_{s} is the total thermal diffusivity $K/c_{\mathrm{P}}\rho$ from $r = r_{\mathrm{s}}$. The hydrostatic solution is Schwarzschild-unstable only in a thin layer near the surface (see e.g., Barekat & Brandenburg 2014; Brandenburg 2016) which is why the Rayleigh number is evaluated at r_{s}. Moreover, χ_{SGS} does not contribute to Ra because it only acts on deviations from the spherically symmetric specific entropy. Additionally, a turbulent Rayleigh number is quoted,

$$\mathrm{Ra_t} = \frac{GM(\Delta r)^4}{\nu \chi_{\mathrm{tot}} R^2} \left(-\frac{1}{c_{\mathrm{P}}} \frac{\mathrm{d}\langle s \rangle_{\theta\phi}}{\mathrm{d}r} \right)_{r_{\mathrm{s}}}, \qquad (15)$$

where $\langle s \rangle_{\theta\phi}$ is the time- and horizontal average of the specific entropy, and $\chi_{\mathrm{tot}} = \chi_{\mathrm{SGS}} + \langle \chi \rangle_{\theta\phi}$ is the total thermal diffusivity. $\mathrm{Ra_t}$ is always significantly smaller than Ra because $\chi_{\mathrm{SGS}} \gg \chi$.

The magnitude of the rotation is controlled by the Taylor number,

$$\mathrm{Ta} = \frac{4\Omega_0^2 (\Delta r)^4}{\nu^2}. \qquad (16)$$

The fluid and magnetic Reynolds numbers and the Péclet number are given by

$$\mathrm{Re} = \frac{u_{\mathrm{rms}}}{\nu k_1}, \quad \mathrm{Re_M} = \frac{u_{\mathrm{rms}}}{\eta k_1}, \quad \mathrm{Pe} = \frac{u_{\mathrm{rms}}}{\chi_{\mathrm{SGS}} k_1}, \qquad (17)$$

respectively, where $u_{\mathrm{rms}} = \sqrt{\frac{3}{2}(U_r^2 + U_\theta^2)}$ is the time- and volume-averaged rms velocity, where U_ϕ^2 has been replaced by $(U_r^2 + U_\theta^2)/2$ to avoid contributions from differential rotation. The inverse of the wavenumber $k_1 = 2\pi/\Delta r \approx 21/R$ is used to characterize the radial extent of the convection zone. Several definitions of the Coriolis number that describes the rotational influence on the flow are discussed in Sect. 3.2.

Mean quantities are denoted by overbars and are defined by the time- and azimuthal average,

$$\overline{f}(r,\theta) = \frac{1}{\Delta\phi \Delta t} \int_{t_0}^{t_0+\Delta t} \int_0^{\Delta\phi} f(r,\theta,\phi,t) \mathrm{d}\phi \mathrm{d}t, \qquad (18)$$

where t_0 and Δt are the beginning and the length of the statistically steady part of the simulation, and where $\Delta\phi = \pi/2$ is the azimuthal extent of the simulation domain. Error estimates were obtained by dividing the time series into three parts and by computing averages over each one of them. The largest deviation of these sub-averages from the average over the whole time series was taken to represent the error.

2.2. Initial and boundary conditions

Initially, the stratification is isentropic with a polytropic index $n = 1.5$ and $\xi_0 = 0.02$, resulting in an initial density contrast of 30. The value of K_0 is chosen such that $F_{\mathrm{rad}} = F_{\mathrm{tot}}$ at the bottom of the domain.

The radial and latitudinal boundaries are assumed to be impenetrable and stress-free for the flow. At the bottom boundary, a fixed heat flux is prescribed, while at the top, a black-body condition is applied. At the latitudinal boundaries, the gradients of thermodynamic quantities are set to zero; see Käpylä et al. (2013). For the magnetic field, we apply a radial field condition at the upper and a perfect conductor condition at the lower boundary. At the latitudinal boundaries, the field is assumed to be tangential to the boundary. These conditions are given in terms of the magnetic vector potential by

$$A_r = 0, \quad \frac{\partial A_\theta}{\partial r} = -\frac{A_\theta}{r}, \quad \frac{\partial A_\phi}{\partial r} = -\frac{A_\phi}{r} \quad (r = R), \qquad (19)$$

$$\frac{\partial A_r}{\partial r} = A_\theta = A_\phi = 0 \quad (r = r_{\mathrm{in}}), \qquad (20)$$

$$A_r = \frac{\partial A_\theta}{\partial \theta} = A_\phi = 0 \quad (\theta = \theta_0, \pi - \theta_0). \qquad (21)$$

The azimuthal direction is periodic for all quantities. The velocity and magnetic fields were initialized with random low-amplitude Gaussian noise fluctuations.

3. Results

Three sets of simulations were run, where $\mathrm{Pr_{SGS}} = 0.1$ (set P01), 1 (P1), and 10 (P10), respectively. The first two sets contain hydrodynamic and MHD runs, and a subset of the MHD runs was remeshed to higher resolution and to correspondingly higher Rayleigh, Péclet, and Reynolds numbers; see Table 1. Only MHD variants of the P10 runs were run.

3.1. Thermal relaxation and convergence

Before discussing the main results, we briefly describe the measures we undertook to ensure that the simulations are thermally relaxed and that the results converged. The relevant timescale for thermal relaxation is the Kelvin-Helmholtz timescale, which is estimated as

$$\tau_{\mathrm{KH}} = \frac{\mathcal{E}_{\mathrm{th}}}{L}, \qquad (22)$$

where $\mathcal{E}_{\mathrm{th}} = \int_V E_{\mathrm{th}} \mathrm{d}V$ is the total thermal energy of the initial non-convecting state, with $E_{\mathrm{th}} = \rho e$, and where $e = c_V T$ is the specific internal energy. In general, the runtime of the simulations, Δt, needs to be of the order of τ_{KH} to ensure thermal relaxation. A shorter runtime suffices if the initial condition is close to the final thermally relaxed convecting state. However, this can typically be concluded only a posteriori.

The normalized Kelvin-Helmholtz timescale in the current simulations is $\tilde{\tau}_{\mathrm{KH}} = \tau_{\mathrm{KH}}/\tau_{\mathrm{ff}} \approx 4.1 \times 10^3$, where $\tau_{\mathrm{ff}} = \sqrt{GM/R^3}$ is the free-fall time. By virtue of the enhanced luminosity

Table 1. Summary of the runs.

Run	Pr_{SGS}	$Ta[10^6]$	Co	Co_ℓ	Co_ω	$Co_\star$	Re	Pe	Re_M	$Ra_t\ [10^6]$	DR	$\Delta\tilde{t}\ [10^3]$
P01-1H	0.1	2.6	1.14	1.10	0.59	0.38	36	3.6	–	0.17	AS	12.6
P01-2H	0.1	3.1	1.25	1.15	0.63	0.42	36	3.6	–	0.19	AS	9.05
P01-3H	0.1	3.7	1.34	1.21	0.66	0.46	37	3.7	–	0.21	(AS)	8.66
P01-4H	0.1	4.4	1.42	1.22	0.67	0.50	37	3.7	–	0.23	(AS)	9.78
P01-5H	0.1	5.1	1.50	1.28	0.70	0.54	38	3.8	–	0.25	(SL)	6.58
P01-6H	0.1	5.8	1.65	1.36	0.75	0.58	37	3.7	–	0.27	SL	5.96
P01-1M	0.1	2.6	1.21	1.12	0.62	0.38	34	3.4	34	0.19	AS	7.29
P01-1Mh	0.1	28.8	1.25	0.85	0.50	0.38	109	11	109	2.18	AS	2.98
P01-2M	0.1	3.1	1.29	1.17	0.65	0.42	35	3.5	35	0.20	AS	4.88
P01-2Mh	0.1	34.9	1.33	0.74	0.40	0.42	113	11	113	2.44	(SL)	3.40
P01-3M	0.1	3.7	1.35	1.20	0.66	0.46	36	3.6	36	0.21	AS	6.33
P01-3Mh	0.1	41.5	1.49	0.80	0.43	0.46	110	11	110	2.59	SL	5.72
P01-4M	0.1	4.4	1.48	1.24	0.70	0.50	36	3.6	60	0.24	(SL)	4.46
P01-5M	0.1	5.1	1.59	1.33	0.75	0.54	36	3.6	51	0.26	SL	3.98
P01-6M	0.1	5.8	1.92	1.54	0.84	0.58	32	3.2	53	0.28	SL	3.56
P1-1H	1.0	2.6	1.31	1.00	0.55	0.38	31	31	–	1.45	AS	12.0
P1-2H	1.0	3.1	1.48	1.13	0.61	0.42	30	30	–	1.47	AS	7.44
P1-3H	1.0	3.7	1.63	1.15	0.64	0.46	30	30	–	1.70	AS	12.0
P1-4H	1.0	4.4	1.80	1.21	0.68	0.50	30	30	–	1.84	AS	7.71
P1-5H	1.0	5.1	1.97	1.25	0.73	0.54	29	29	–	2.01	SL	9.45
P1-6H	1.0	5.8	2.14	1.32	0.78	0.58	29	29	–	2.13	SL	9.44
P1-1M	1.0	2.6	1.42	0.98	0.58	0.38	29	29	29	1.59	AS	6.65
P1-2M	1.0	3.1	1.58	1.08	0.63	0.42	28	28	28	1.66	AS	7.18
P1-2Mh	1.0	34.9	1.56	0.68	0.38	0.42	96	96	96	19.9	(SL)	4.41
P1-3M	1.0	3.7	1.72	1.13	0.67	0.46	29	29	29	1.77	AS	5.84
P1-3Mh	1.0	41.5	1.73	0.74	0.41	0.46	94	94	94	20.9	SL	5.46
P1-4M	1.0	4.4	1.87	1.20	0.71	0.50	28	28	28	1.92	SL	5.69
P1-5M	1.0	5.1	2.03	1.26	0.76	0.54	28	28	28	2.03	SL	6.40
P1-6M	1.0	5.8	2.19	1.33	0.80	0.58	28	28	28	2.12	SL	5.90
P10-1M	10	2.6	1.75	0.99	0.58	0.38	23	233	23	13.4	AS	4.53
P10-2M	10	3.1	1.98	1.06	0.64	0.42	23	227	23	14.4	AS	4.36
P10-3M	10	3.7	2.16	1.16	0.70	0.46	23	227	23	15.0	AS	4.41
P10-4M	10	4.4	2.31	1.26	0.74	0.50	23	229	23	15.1	AS	5.90
P10-5M	10	5.1	2.53	1.31	0.80	0.54	23	226	23	16.3	(AS)	4.36
P10-6M	10	5.8	2.68	1.40	0.84	0.58	23	228	23	16.7	(SL)	5.69
P10-7M	10	6.6	2.80	1.46	0.88	0.62	23	234	23	16.9	(AS)	3.50
P10-8M	10	7.5	3.10	1.56	0.95	0.65	22	224	22	17.7	SL	3.53
P10-9M	10	8.4	3.28	1.62	1.00	0.69	22	228	22	18.1	SL	7.03

Notes. Hydrodynamic (MHD) runs are denoted by the suffix H (M). Most of the runs use a grid resolution $128\times288\times144$, the exception being runs denoted by the suffix h, where resolution $256\times576\times288$ was used. The Rayleigh number in most runs is 7.0×10^8, expect in the higher-resolution runs, denoted by suffix h, where it is $Ra = 2.4\times10^9$. Co, Co_ℓ, Co_ω, and $Co_\star$ denote the definitions of the Coriolis number given by Eqs. (25), (27), (28), and (30). $Pr_M = 1$ in all runs except in P01-4M and P01-6M where $Pr_M = 1.67$, and in P01-5M where $Pr_M = 1.43$ to obtain growing dynamos. The penultimate column denotes the type of differential rotation with parenthesis indicating that the result is not statistically significant. The last column denotes the length of the time averages in units of $10^3\tau_{ff}$.

method used here (see e.g., Käpylä et al. 2020), τ_{KH} can be resolved in the simulations; see the 13th column of Table 1. In the hydrodynamical simulations, the initial transient, data from which is not used in the time-averaging, is typically of the order of τ_{KH}; see Fig. 1a for data from run P1-6H. Hydrodynamic simulations were considered thermally relaxed when the volume-averaged (denoted by angle brackets) total energy density $\langle E_{tot}\rangle$ reaches a statistically steady state, where $\langle E_{tot}\rangle = \langle E_{th}\rangle + \langle E_{pot}\rangle + \langle E_{kin}\rangle + \langle E_{mag}\rangle$ with $E_{pot} = \rho\phi$, $E_{kin} = \frac{1}{2}\rho U^2$, and $E_{mag} = \frac{1}{2}\mu_0^{-1}B^2$. The flows often reach a statistically steady state already significantly earlier; see the inset of Fig. 1a for representative results for the time evolution of the rms value of U_ϕ from run P1-6H.

The MHD simulations were typically started from thermally relaxed hydrodynamic cases. In these cases, the transient due to thermal relaxation is significantly shorter than in the hydrodynamic progenitor run. However, the growth of the magnetic field is slow at the modest magnetic Reynolds numbers presented here. Therefore, another two-phase transient follows, in which the magnetic field first grows from a weak seed field to become dynamically important, which is followed by a period in which the thermal state relaxes toward a new statistically steady MHD state; see Fig. 1b. Again, the criterion for convergence is taken to be that the sum of the volume-averaged total energy density $\langle E_{tot}\rangle$ settles to a new statistically steady state. In some cases, such as in run P1-6M
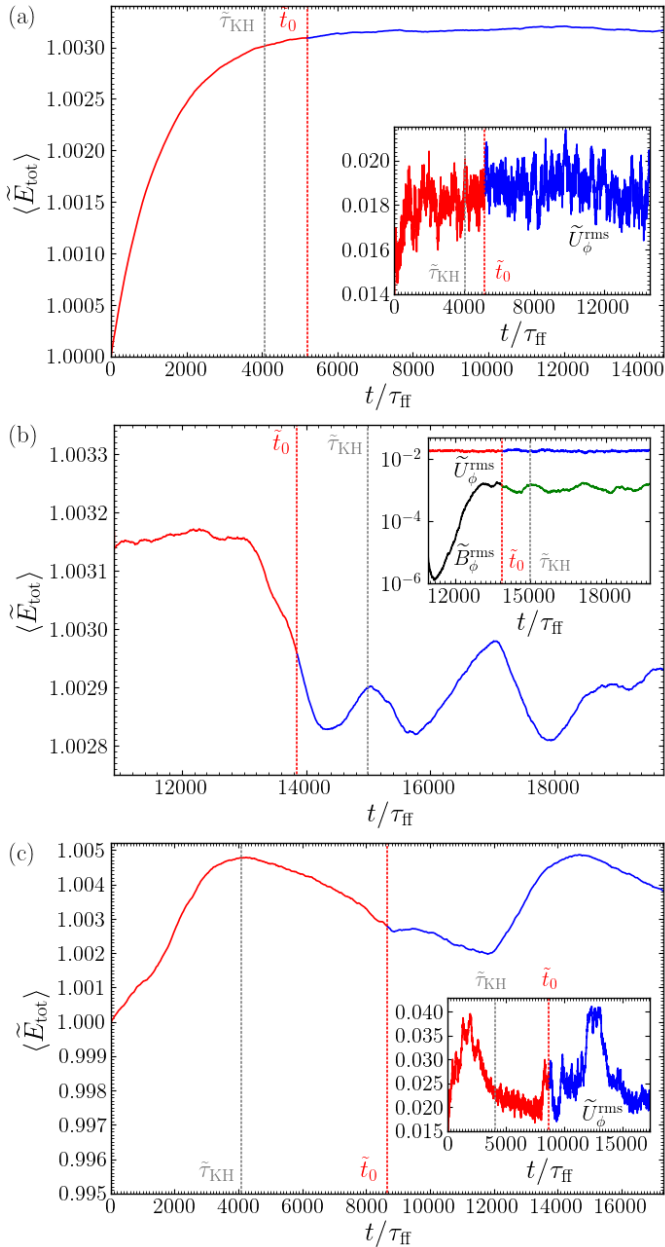
Fig. 1. Time series of total energy density and the rms velocity and magnetic fields. (*a*) Volume-averaged total energy density $\langle \widetilde{E}_{\text{tot}} \rangle$ normalized by its value at $t = 0$ from run P1-6H. The inset shows the volume-averaged rms value of the azimuthal flow $\widetilde{U}_\phi^{\text{rms}} = U_\phi^{\text{rms}} / \sqrt{GM/R}$. The red (blue) part of the curve indicates the transient (statistically stationary) part of the time series, where $\tilde{t}_0 = t_0/\tau_{\text{ff}}$ indicates the starting time for the time averaging. τ_{KH} indicates the Kelvin-Helmholtz timescale. (*b*) Same as above, but for the corresponding MHD run P1-6M. The inset shows $\widetilde{B}_\phi^{\text{rms}} = B_\phi^{\text{rms}}/(\rho_0\mu_0 \sqrt{GM/R})$ in addition to $\widetilde{U}_\phi^{\text{rms}}$. The black (green) parts of the data for $\widetilde{B}_\phi^{\text{rms}}$ indicate transient (statistically stationary) parts. (*c*) Same as panel a, but for run P01-3H.

shown in Fig. 1b, the total energy density in the MHD state still shows temporal modulation due to quasi-cyclic large-scale magnetism.

However, in a few of hydrodynamic cases (runs P01-2H, P01-3H, and P01-4H), a statistically stationary state was not reached, even though these models were run several Kelvin-Helmholtz times; see Fig. 1c. These runs exhibit excursions between different flow states where the mean azimuthal flow

also shows sign changes, leading to a large uncertainty in the estimates of differential rotation. The most probable explanation for this behaviour is that these models lie in a bistable parameter regime in which different differential rotation profiles, including AS and SL states, are possible, depending on the history of the run (Gastine et al. 2014; Käpylä et al. 2014). Whether these models finally settle to one or the other stable solution is unclear and would possibly require significantly longer integration times. None of the corresponding MHD runs exhibits similar excursions, thus being consistent with the absence of hysteresis in the MHD regime (Karak et al. 2015).

3.2. Differential rotation and meridional circulation

The main focus of the current study is to explore the effects of the Prandtl number for the large-scale flows that develop in rotating convective systems. The mean rotation profile is given by the time and azimuthal average,

$$\overline{\Omega}(r,\theta) = \Omega_0 + \frac{\overline{U}_\phi(r,\theta)}{r\sin\theta}, \tag{23}$$

and the meridional flow is given by $\overline{\boldsymbol{U}}_{\text{mer}} = (\overline{U}_r, \overline{U}_t, 0)$. In many simulations, the latitudinal profiles of $\overline{\Omega}$ are non-monotonic such that the rotation rate has a polar jet, a maximum at mid-latitudes, or sometimes several local minima and maxima as a function of latitude. Furthermore, equatorial asymmetries can occur, rendering the amplitude of the latitudinal shear an unreliable diagnostic of the overall sense of differential rotation; see representative examples in Figs. 2–4. Therefore the classification of the AS and SL rotation profile is here based on the mean rotation profile at the equator

$$\langle \Delta\tilde{\Omega}_{\text{eq}} \rangle = \frac{\int_{r_{\text{in}}}^R r^2 [\overline{\tilde{\Omega}}(r,\theta_{\text{eq}}) - 1]\mathrm{d}r}{\int_{r_{\text{in}}}^R r^2\,\mathrm{d}r}, \tag{24}$$

where $\theta_{\text{eq}} = \pi/2$, and where the tildes refer to normalization by the rotation rate of the frame of reference, Ω_0. If $\langle \Delta\tilde{\Omega}_{\text{eq}} \rangle > 0$ ($\langle \Delta\tilde{\Omega}_{\text{eq}} \rangle < 0$), the run is classified as SL (AS) rotator. This measure turns out to be a monotonic function of rotation and is furthermore much less affected by equatorial asymmetries or polar jets. See Camisassa & Featherstone (2022) for a more granular classification making use of more diagnostics to describe the transition.

The current results indicate that the convective velocity increases when the Prandtl number is decreased. This is manifest when the fluid Reynolds number increases for a decreasing SGS Prandtl number; see the eighth column of Table 1. Naively, it might then be expected that achieving SL differential rotation for low Pr_{SGS} would be more difficult, that is, require faster rotation. The rotational influence on the flow is often quantified by a simple definition of the Coriolis number,

$$\text{Co} = \frac{2\,\Omega_0}{u_{\text{rms}}k_1}, \tag{25}$$

where the convective length scale is assumed to be unchanged by rotation. When this definition is used to characterize the results, the Coriolis number at which the rotation profile flips from AS to SL decreases monotonically with Pr_{SGS}; see Fig. 5a where $\langle \Delta\tilde{\Omega}_{\text{eq}} \rangle$ is shown for all runs as a function of Co. That is, in the low-resolution MHD runs with $\text{Pr}_{\text{SGS}} = 0.1$ (1), the transition occurs around Co ≈ 1.5 (Co ≈ 1.8); see Figs. 2 and 3, whereas
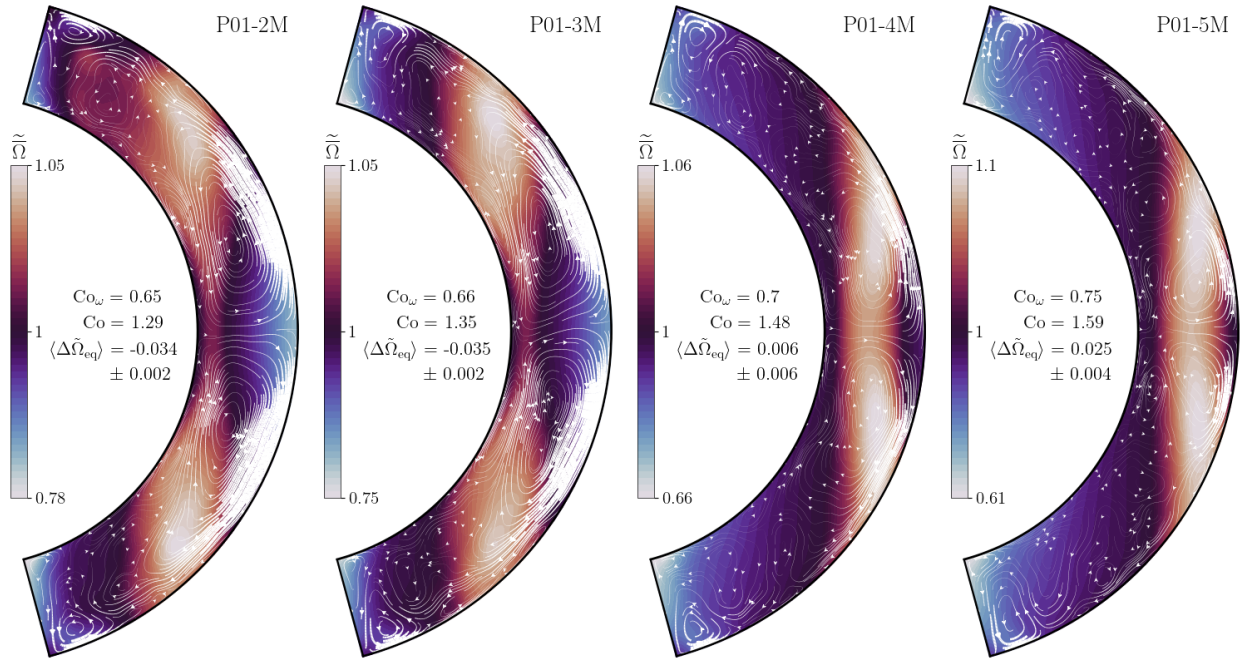
Fig. 2. Time-averaged rotation profiles from MHD runs P01-[2-5]M near the AS-SL transition with $\mathrm{Pr_{SGS}} = 0.1$ with the rotation rate increasing from left to right. Coriolis numbers according to Eqs. (25) and (28) and the mean differential rotation at the equator $\langle \Delta\tilde{\Omega}_{eq} \rangle$ according to Eq. (24) are indicated in each panel. The white arrows indicate the meridional flow.
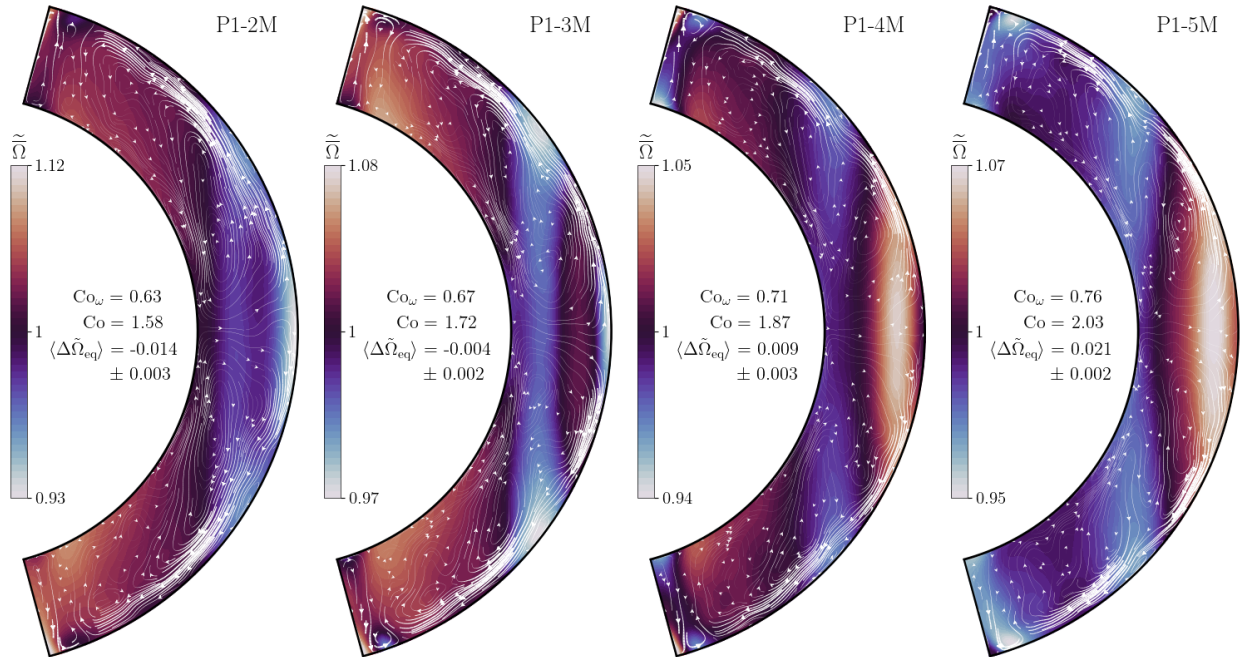

Fig. 3. Same as Fig. 2 but for runs P1-[2-5]M in set P1.

for $\mathrm{Pr_{SGS}} = 10$ the transition occurs at an even higher Coriolis number ($\mathrm{Co} \approx 3$); see Fig. 4.

However, the validity of this simplistic definition of the Coriolis number in characterizing the simulations can be questioned based on its very crude estimate of the convective length scale and velocity amplitude. For example, Gastine et al. (2014) argued that a local Rossby (inverse Coriolis) number based on the length scale from the mean spherical harmonic degree $\overline{\ell}_u$ of

the $m \neq 0$ poloidal flows gives a more accurate estimate (see also Schrinner et al. 2012). Furthermore, they showed that the scatter near the AS-SL transition is reduced with this definition, essentially reducing the apparent dependence on Prandtl number significantly. Here this was tested by computing $\overline{\ell}_u$ according to

$$\overline{\ell}_u = \sum_{\ell} \ell \frac{\langle \boldsymbol{U}_p^{\ell} \cdot \boldsymbol{U}_p^{\ell} \rangle}{\langle \boldsymbol{U}_p \cdot \boldsymbol{U}_p \rangle}, \tag{26}$$
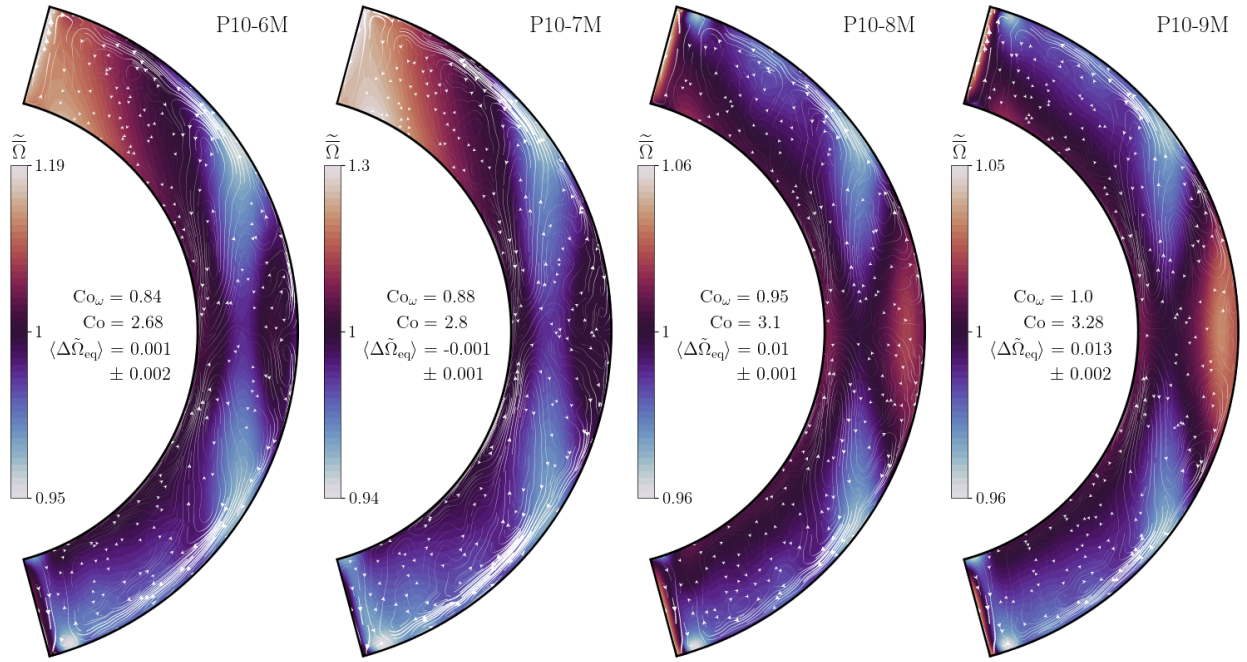
Fig. 4. Same as Fig. 2 but for runs P10-[6-9]M in set P10.

where $\boldsymbol{U}_p$ is the non-axisymmetric poloidal flow, and where ℓ is the spherical harmonic degree. Data from a varying number of horizontal slices from near the base, at the middle, and near the top of the CZ were analyzed for each run, and the resulting $\bar{\ell}_u$ is an average over the depths and time. The number of time slices per run varies between 7 and roughly 60. The corresponding length scale is $d_u = \pi \Delta R / \bar{\ell}_u$, and the Coriolis number based on this is given by

$$\mathrm{Co}_\ell = \frac{2\Omega_0 d_u}{u_{\mathrm{rms}}}, \tag{27}$$

where u_{rms} is defined in the same way as in Eq. (17). The numbers in Table 1, fifth column, indicate that the value of Co_ℓ is sensitive to the Reynolds number such that in the runs with the highest Re, the values of Co_ℓ are roughly 30% lower than those of the low-resolution runs. Similarly, a Coriolis number based on fluctuating vorticity can be defined as (e.g., Brun et al. 2022)

$$\mathrm{Co}_\omega = 2\Omega_0 / \omega'_{\mathrm{rms}}, \tag{28}$$

where $\omega' = \nabla \times \boldsymbol{u}$ with $\boldsymbol{u} = \boldsymbol{U} - \overline{\boldsymbol{U}}$. This quantity shows a similar sensitivity to the fluid Reynolds number as Co_ℓ; see the sixth column of Table 1. Both of these definitions pick up smaller length scales at the highest Reynolds number runs, resulting in lower Coriolis numbers. This is likely an indication that the simulations are still far away from an asymptotic regime in which the results would be independent of the diffusivities. Nevertheless, Co_ℓ and Co_ω characterize the rotational influence on the flow more accurately than Co by being sensitive to the actual dominant length scale. However, due to the Reynolds number sensitivity, we should only compare results from runs with comparable Re when these definitions are used to characterize the results.

The average radial differential rotation at the equator is shown as functions of Co_ℓ and Co_ω in Figs. 5b and c, respectively. When the five runs at higher Reynolds and Péclet numbers are ignored for the time being, these results suggest that the dependence of the differential rotation transition as a function of the Prandtl number all but vanishes for $\mathrm{Pr}_{\mathrm{SGS}} < 1$. However, in both cases, the transition for $\mathrm{Pr}_{\mathrm{SGS}} = 10$ still occurs at a higher Co_ℓ and Co_ω than for the $\mathrm{Pr}_{\mathrm{SGS}} = 0.1$ and 1 cases[2]. These results agree with those reported by Karak et al. (2018), who also found that a Prandtl number above unity promotes AS differential rotation due to enhanced downward angular momentum transport. Both definitions give much lower Coriolis numbers for the higher-Re runs because smaller convective scales are resolved and $\bar{\ell}_u$ and ω' pick these up. Furthermore, among the five higher-Re runs, the single AS model (P01-1Mh) appears to have a marginally larger Coriolis number than the SL counterparts in both cases, although the error estimates for Co_ℓ and Co_ω are large in both cases. Whether this is a real effect or due to insufficient statistics remains open at this point. As a side note, the resemblance of Figs. 5b and c, or alternatively, the correlation between Co_ω and Co_ℓ, suggests that Co_ω captures the rotation dependence of the convective length scale almost as well as Co_ℓ without having to perform numerically expensive spherical harmonic decomposition.

Each of the definitions of the Coriolis number discussed so far rely on diagnostic quantities such as u_{rms}, $\bar{\ell}_u$, and ω', that are sensitive to other details, such as the fluid Reynolds number, of the system. Yet another alternative is to define a Coriolis number that depends only on stellar input parameters such as the luminosity, mass, and rotation rate of the modeled star. This can be constructed by assuming that

$$L = \rho_\star u_\star^3 R^2, \tag{29}$$

where $L = 4\pi r_{\mathrm{in}}^2 F_{\mathrm{bot}}$ is the luminosity, $\rho_\star$ is a reference density, and $u_\star$ is an estimate of an average convective velocity. We

---

[2] Only the two most rapidly rotating runs with $\mathrm{Pr}_{\mathrm{SGS}} = 10$ have statistically significant SL differential rotation; see the 12th column of Table 1.

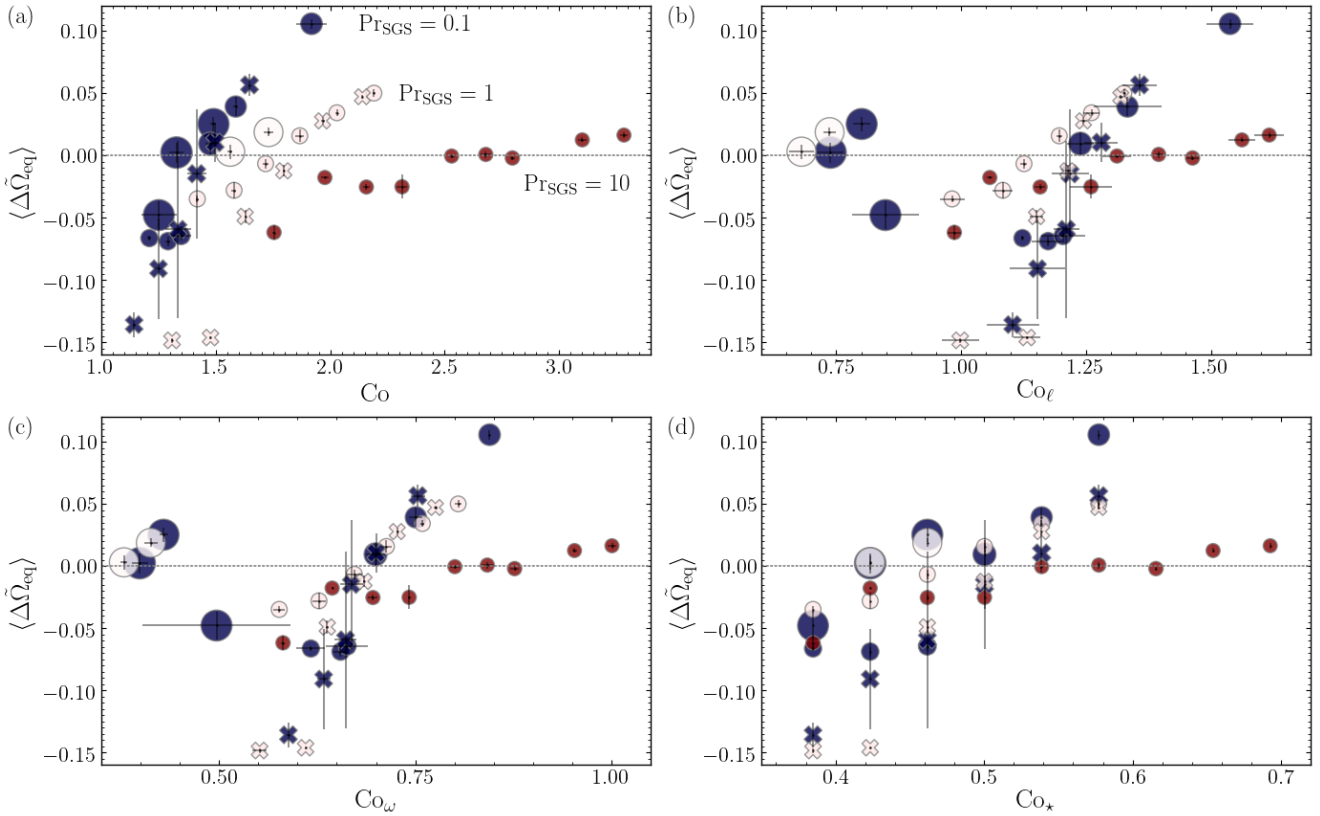**Fig. 5.** Normalized average angular velocity at the equator $\langle \Delta \tilde{\Omega}_{eq} \rangle$ for all runs as a function of Co *(a)*, Co_ℓ *(b)*, Co_ω *(c)*, and $Co_\star$ *(d)*. Circles (crosses) denote MHD (hydrodynamic) runs, and the colour of the symbols indicates the SGS Prandtl number. The sizes of the symbols are proportional to Re_M (Re) for MHD (hydrodynamic) runs.

assume $\rho_\star = \rho_0$[3] and construct a stellar Coriolis number

$$Co_\star = \frac{2\Omega_0 R}{u_\star} = \frac{2\Omega_0 R^{5/3}\rho_0^{1/3}}{L^{1/3}}. \tag{30}$$

While this definition is imperfect in the sense that the actual convective flow speed or scale do not enter, it is useful to determine whether a model with a given rotation rate and luminosity is an AS or SL rotator. This makes particularly sense in the homogeneous set of simulations considered here, where the stellar mass, luminosity, and radius are all fixed. The results are shown in Fig. 5d. It is apparent that the runs with $Pr_{SGS} = 10$ require a significantly higher $Co_\star$, corresponding here to higher Ω_0, to achieve SL differential rotation. However, the AS-SL transition occurs at the same $Co_\star$ for $Pr_{SGS} = 1$ and 0.1. Notably, the MHD runs at $Pr_{SGS} = 0.1$ and 1 for $Co_\star = 0.50$ are at least marginally SL in comparison to the corresponding AS hydrodynamic cases. Similarly, the higher-resolution runs are SL or marginally SL for $Co_\star = 0.46$, whereas the corresponding lower-resolution MHD and hydrodynamic runs are all AS. The current higher-resolution runs with $Re_M \approx 94 \dots 113$ also have small-scale dynamos, which was tested with separate runs where the axisymmetric ($m = 0$) magnetic fields were suppressed. Therefore, it is plausible that the main contribution to the earlier appearance of SL differential rotation in these cases is due to the growing importance of the magnetic fields. However, no corresponding higher-resolution hydrodynamic runs were made to confirm this. The

current results agree with the results of Hotta & Kusano (2021) and Hotta et al. (2022), who argue in favour of the magnetic field being the decisive factor in the transition. Finally, when the simulations are scaled to physical units as in Käpylä et al. (2020), the lowest value in the present study, $Co_\star = 0.38$, corresponds to the case of solar rotation rate at solar luminosity.

The conclusion of comparing the results characterized in terms of the four variants of the Coriolis number is that SL differential rotation is substantially more difficult to obtain for $Pr_{SGS} = 10$ than for $Pr_{SGS} = 1$ and 0.1, whereas in the latter two cases, there is no clear difference. Furthermore, the use of the simplistic Coriolis number, Eq. (25), gives misleading results and should be avoided. In contrast to the SGS Prandtl number, the dependence on magnetic fields is clearer, such that in MHD runs, SL differential rotation is easier to excite.

3.3. Angular momentum transport

The angular momentum in the interior of the star is governed by the conservation equation

$$\frac{\partial}{\partial t}(\overline{\rho}\mathcal{L}) + \nabla \cdot \boldsymbol{\mathcal{T}} = 0, \tag{31}$$

where $\mathcal{L} = \varpi^2 \overline{\Omega}$ is the specific angular momentum, with $\varpi = r \sin\theta$ being the lever arm, and where

$$\boldsymbol{\mathcal{T}} = \varpi[\overline{\rho u u_\phi} + \overline{\rho}\overline{U}(\overline{U}_\phi + \varpi\Omega_0) \\ - (\overline{b b_\phi} + \overline{B}\,\overline{B}_\phi)/\mu_0 - 2\nu\overline{\rho}\overline{\mathbf{S}} \cdot \hat{\boldsymbol{\phi}}], \tag{32}$$

is the flux of angular momentum, where $\boldsymbol{u} = \boldsymbol{U} - \overline{\boldsymbol{U}}$ and $\boldsymbol{b} = \boldsymbol{B} - \overline{\boldsymbol{B}}$ are the fluctuating velocity and magnetic field, and where $\hat{\boldsymbol{\phi}}$ is the

---

[3] Using the average density of the star, $\rho_{av} = M/\frac{4}{3}\pi R^3$, is another option, and in that case, the definition of $Co_\star$ is fully determined by the stellar parameters.
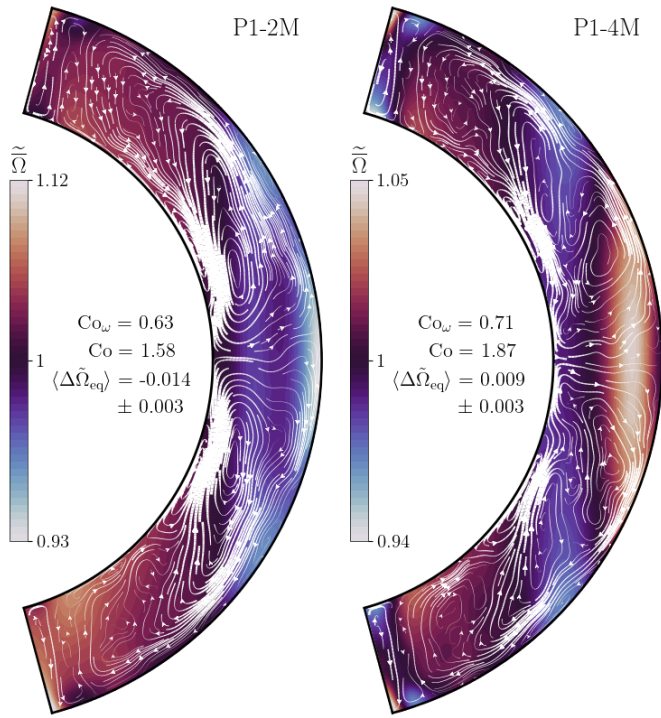
Fig. 6. Total angular momentum flux $\mathcal{T}$ (arrows) superimposed on the mean angular velocity profile (colour contours) from runs P1-2M and P1-4M.

unit vector in the azimuthal direction. The internal angular velocity profile is thus determined by the spatial distribution of the angular momentum fluxes. The main transporters are due to the Reynolds and Maxwell stress due to fluctuating and mean flows and fields (see Rüdiger 1989; Rüdiger & Hollerbach 2004),

$$\mathcal{T}^{u} = \varpi \overline{Q}^{u} = \varpi \overline{\rho u u_{\phi}}, \tag{33}$$

$$\mathcal{T}^{b} = \varpi \overline{M}^{b} = -\varpi \overline{b b_{\phi}}/\mu_{0}, \tag{34}$$

$$\mathcal{T}^{\overline{U}} = \varpi \overline{Q}^{\overline{U}} = \varpi \overline{\rho} \overline{U}(\overline{U}_{\phi} + \varpi \Omega_{0}), \tag{35}$$

$$\mathcal{T}^{\overline{B}} = \varpi \overline{M}^{\overline{B}} = -\varpi \overline{B}\,\overline{B}_{\phi}/\mu_{0}. \tag{36}$$

Additionally, the contributions to the stress due to molecular viscosity are given by

$$\mathcal{T}^{\nu} = \varpi \overline{Q}^{\nu} = -2\varpi \nu \overline{\rho} \overline{\mathbf{S}} \cdot \hat{\boldsymbol{\phi}}. \tag{37}$$

Although the viscous flux is negligibly small in the Sun, it is typically non-negligible in simulations (e.g., Guerrero et al. 2022). Representative results of $\mathcal{T}$ are shown in Fig. 6 superimposed on top of the angular velocity in runs P1-2M and P1-4M. The total angular momentum flux closely follows the pattern of the meridional circulation; see also Fig. 3. To see which terms dominate the angular momentum transport, we proceed to compute the divergences of the various terms that are encapsulated in $\mathcal{T}$. Figure 7 show the divergences of the various contributions to the angular momentum flux given by Eqs. (33)–(37) for runs P1-2M and P1-4M. The contributions due to the turbulent Reynolds stress $\overline{Q}^{u}$ and due to the meridional flow $\overline{Q}^{U}$ are by far the largest and approximately balance out in all of the cases considered here. The viscous and Maxwell stress contributions are clearly subdominant. The former (latter) decreases (increases) in

the higher-resolution runs, but $\overline{M}^{b}$ remains subdominant in these cases as well. The rightmost panels of Fig. 7 show the residual divergence $\nabla \cdot \mathcal{T}$, which has relatively high peak values, but primarily on small scales.

Because the divergence of the stress is very similar in the AS and SL cases, the difference in the angular momentum transport between these cases is rather subtle. Furthermore, the stress from meridional circulation is radially outward near the equator in both AS and SL cases; see for example Fig. 3, and the viscous and magnetic contributions are weak in all of the current runs. Therefore the most plausible explanation is a change in the turbulent Reynolds stress $\mathcal{T}^{u}$, which is shown in Fig. 8 for runs P1-2M and P1-4M superimposed on the mean angular velocity. The turbulent Reynolds stress is nearly radially downward at high latitudes in the bulk of the CZ. The region of downward radial flux is roughly confined inside the tangent cylinder in all cases. Outside the tangent cylinder and near the surface at all latitudes, $\mathcal{T}^{u}$ is directed predominantly equatorward regardless of whether the rotation profile is AS or SL. Outside the tangent cylinder, the angular momentum transport is increasingly axial, although the radial flux at the equator remains non-zero in all cases. The sense of the differential rotation is related to the sign of the radial component of $\mathcal{T}^{u}$ at the equator: for positive (outward) $\mathcal{T}^{u}$, the differential rotation is SL (run P1-4M in Fig. 8), whereas it is AS for negative (downward) $\mathcal{T}^{u}$ (run P1-2M). Therefore, it appears sufficient to study the equatorial radial angular momentum flux to determine the difference between AS and SL differential rotation.

To study the equatorial Reynolds stress in more detail, a number of slices of the $m \neq 0$ velocity field $U(r, \theta_{eq}, \phi)$ were analyzed. Azimuthal Fourier filtering was applied to produce filtered velocity fields $U^{f}(m_1', m_2')$, where azimuthal orders ranging between m_1' and m_2' were retained[4]. These flows are used to compute the radial Reynolds stress,

$$\overline{Q}^{u}_{r\phi}(m_1', m_2') = \frac{1}{\Delta\phi\Delta t} \int_{t_0}^{t_0+\Delta t} \int_{0}^{\Delta\phi} \rho U^{f}_r(m_1', m_2') U^{f}_{\phi}(m_1', m_2') \mathrm{d}\phi \mathrm{d}t. \tag{38}$$

Here the density fluctuations are assumed to be small, and no filtering was applied to ρ. Representative results are shown in Fig. 9. In the AS case P1-2M, Fig. 9a, the total Reynolds stress is negative everywhere except at the base of the CZ. Contributions from the largest scale ($m_1', m_2' = 1, 2$) non-axisymmetric motions are statistically almost identical with the total stress. A weak positive contribution around the middle of the CZ is visible for ($m_1', m_2' = 3, 5$), but the Reynolds stress for ($m_1', m_2' = 1, 5$) is again very similar to the total stress. In the SL runs, the largest scales ($m_1', m_2' = 1, 2$) also contribute to a downward flux, whereas the main contribution to the net outward flux comes from ($m_1', m_2' = 3, 5$); see Fig. 9b for run P1-4M. Similarly to the AS case, the contributions from $m' > 5$ are small. This indicates that practically all of the Reynolds stress at the equator is due to relatively large-scale structures that can be identified as Busse columns (Busse 1970a,b), which are also often referred to as banana cells. Such features are often prominently visible in snapshots of the velocity field; see Fig. 10 for a representative example. The Busse cells are manifestations of non-linear prograde-propagating thermal Rossby waves. It is therefore somewhat questionable to talk about turbulent Reynolds stress in this context since the Busse columns are essentially large-scale convective modes.

---

[4] Due to the $\Delta\phi = \pi/2$ azimuthal extent of the simulation domain, m' corresponds to $4m$ in a full sphere.
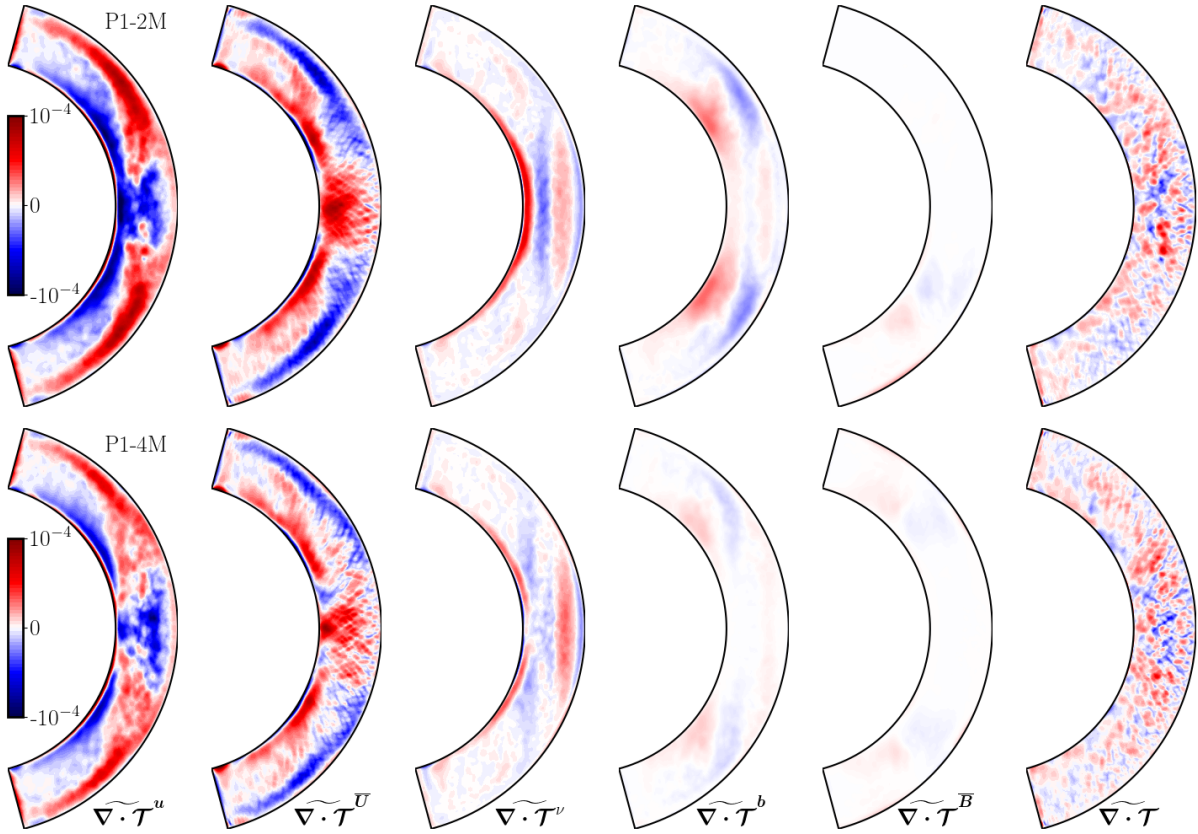
Fig. 7. Divergences of the different contributions to the angular momentum flux, Eqs. (33)–(37), from runs P1-2M (*top row*) and P1-4M (*bottom*). The rightmost panels show the divergence of the total stress, and the tildes refer to normalization by $\rho_0 GM$.
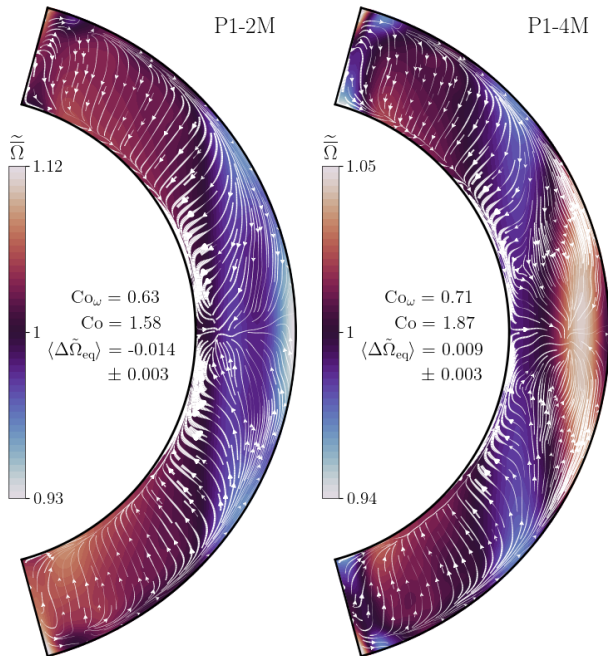

Fig. 8. Same as Fig. 6 but showing the turbulent Reynolds stress $\mathcal{T}^u$.

The mechanism by which the differential rotation is generated in the current simulations is therefore different from that in Hotta et al. (2022), where the small-scale Maxwell stress is the dominant contribution to the radial angular momentum trans-port. While the high-resolution runs in the present study have small-scale dynamos and show an increased tendency for SL differential rotation, the Reynolds stress due to the thermal Rossby waves is still the dominant contribution to the angular momentum flux in all of the runs considered here. In an earlier study (Käpylä et al. 2017), the Maxwell stresses were found to be comparable to the Reynolds stress at the highest magnetic Reynolds numbers, but in that study, the magnetic Prandtl number was higher ($\mathrm{Pr_M} = 5$), and the modelled stars typically rotated three to four times faster than in the current study. Although the Maxwell stress dominates the angular momentum transport in the simulations of Hotta et al. (2022), large-scale Busse columns can still be seen in the deep parts of their model; see for example their Fig. 6. If such large-scale convective patters were as prominent in the Sun, they should have been detected by helioseismology, but there is currently no evidence to this effect. Therefore, it seems that although highly magnetized simulations are more solar-like in terms of the rotation profile, the conundrum with the too prominent large-scale structures remains.

Furthermore, in hydrodynamic mean-field theories of differential rotation (e.g., Rüdiger 1989; Kitchatinov & Rüdiger 2005; Rogachevskii & Kleeorin 2015), the turbulence models are necessarily simplified, and large-scale convection modes such as Busse columns do not appear. In the most commonly adopted approach of Kitchatinov & Rüdiger (2005), the radial angular momentum transport at the equator is downward for slow rotation and vanishes for rapid rotation. The SL differential rotation results from a strong equatorward transport. Numerical simulations of isothermal homogeneous anisotropic turbulence also produce downward (slow rotation) or vanishing (rapid rotation) radial angular momentum flux at the equator (Käpylä 2019a)
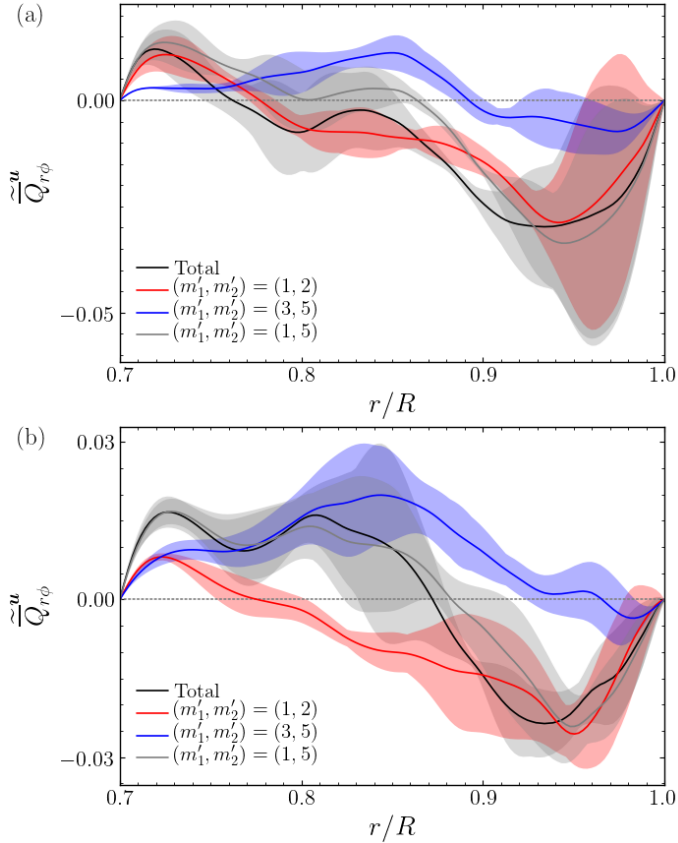
(a)

(b)

Fig. 9. Fourier-filtered and total Reynolds stress component $\widetilde{\overline{Q}}_{r\phi}^{u}$ from runs P1-2M *(a)* and P1-4M *(b)* as indicated in the legend. The shaded areas indicate error estimates according to the definition in Sect. 2.1.

Fig. 10. Instantaneous normalized radial Reynolds stress component $\widetilde{\overline{Q}}_{r\phi}^{u}$ on the equatorial plane from run P01-6M (colour contours). The $m \neq 0$ flows are indicated by the arrows, the width of which is proportional to the local flow amplitude.

in qualitative accordance with Kitchatinov & Rüdiger (2005). Hydrodynamic mean-fields models based on these concepts do not typically produce AS solutions unless strong magnetic fields are present (Kitchatinov & Rüdiger 2004), although more recently, a hydrodynamic mechanism has also been discussed (Rüdiger et al. 2019). This latter process relies on poleward horizontal angular momentum flux at slow rotation, which was also found from local simulations, but which appears to be absent in global models such as those presented here. The mean-field theories avoid the problem of too prominent thermal Rossby waves by simply neglecting them, whereas they fail to characterize both AS and SL cases in the current simulations. This difference is yet another facet of the convective conundrum, the resolution of which is likely to require further critical assessment of both theoretical and simulation approaches.

4. Conclusions

The transition from AS to SL differential rotation was studied as a function of the SGS Prandtl number (Pr_{SGS}). Four definitions of the Coriolis number were used to quantify the exact point of transition from simulations where the rotation of the star was varied. While this transition occurs at a higher Coriolis number for $Pr_{SGS} = 10$ than for $Pr_{SGS} = 1$ and 0.1, no statistically relevant difference was found between the last two cases. This suggests that the Prandtl number dependence of the AS-SL transition is weak for $Pr_{SGS} < 1$, whereas a high Prandtl number makes it significantly more difficult to achieve SL differential rotation.
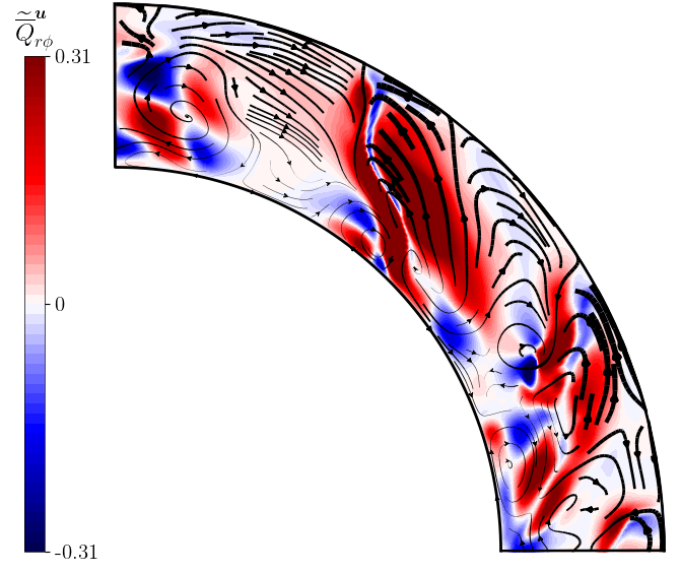
These results are puzzling because earlier non-rotating local simulations (Käpylä 2021) suggested that the cases $Pr = 1$ and $Pr = 0.1$ also differ significantly in many respects. A notable difference to the study of Käpylä (2021) is that the current simulations do not include a radiative layer below the CZ. This can explain why no subadiabatic layers develop at the base of the CZs in the current simulations: the effects of overshooting are absent. The latter was found to be particularly sensitive to the Prandtl number in the local simulations Käpylä (2019b) and Käpylä (2021). The inclusion of a radiative layer has also consequences for the dynamo solutions (e.g., Guerrero & Smolarkiewicz 2016; Käpylä 2022), which also couple back to differential rotation. Furthermore, rotation was not taken into account in the earlier Cartesian studies. These aspects need to be revisited in future studies.

Many of the current simulations also included magnetic fields, but often in a parameter regime in which the small-scale dynamo is not excited. Thus the influence of magnetic fields is relatively weak in most of the current runs. Nevertheless, the magnetic fields make it easier to excite SL differential rotation especially in the current higher-resolution runs, which likely also have small-scale dynamos. However, the effects of magnetic fields are likely to be more significant in higher Re_M systems, as shown in the recent results of Hotta et al. (2022). Therefore, magnetism appears to be the most promising candidate to explain the discrepancy between solar observations and global simulations. Nevertheless, the non-detection of thermal Rossby waves from the Sun, which remain prominent in all current simulations, still raises questions about the generation mechanism of solar differential rotation. Finally, the difference between mean-field theories of differential rotation and 3D simulation results is pointed out as another aspect that requires further scrutiny in the future.

References

Barekat, A., & Brandenburg, A. 2014, A&A, 571, A68

Bekki, Y., Hotta, H., & Yokoyama, T. 2017, ApJ, 851, 74

Brandenburg, A. 2016, ApJ, 832, 6

Brandenburg, A., Nordlund, A., & Stein, R. F. 2000, in Geophysical and Astrophysical Convection, Contributions from a workshop sponsored by the Geophysical Turbulence Program at the National Center for Atmospheric Research, October 1995, eds. P. A. Fox, & R. M. Kerr (The Netherlands: Gordon and Breach Science Publishers), 85

Brun, A. S., Miesch, M. S., & Toomre, J. 2004, ApJ, 614, 1073

Brun, A. S., Strugarek, A., Noraz, Q., et al. 2022, ApJ, 926, 21

Busse, F. H. 1970a, ApJ, 159, 629

Busse, F. H. 1970b, J. Fluid Mech., 44, 441

Camisassa, M. E., & Featherstone, N. A. 2022, ApJ, 938, 65

Cattaneo, F., Brummell, N. H., Toomre, J., Malagoli, A., & Hurlburt, N. E. 1991, ApJ, 370, 282

Dobler, W., Stix, M., & Brandenburg, A. 2006, ApJ, 638, 336

Fan, Y., & Fang, F. 2014, ApJ, 789, 35

Gastine, T., Yadav, R. K., Morin, J., Reiners, A., & Wicht, J. 2014, MNRAS, 438, L76

Gilman, P. A. 1983, ApJS, 53, 243

Guerrero, G., Smolarkiewicz, P. K., Kosovichev, A. G., & Mansour, N. N. 2013, ApJ, 779, 176

Guerrero, G., Smolarkiewicz, P. K., de Gouveia Dal Pino, E. M., Kosovichev, A. G., & Mansour, N. N. 2016, ApJ, 819, 104

Guerrero, G., Stejko, A. M., Kosovichev, A. G., Smolarkiewicz, P. K., & Strugarek, A. 2022, ApJ, 940, 151

Hanasoge, S. M., Duvall, T. L., & Sreenivasan, K. R. 2012, Proc. Natl. Acad. Sci., 109, 11928

Hanasoge, S., Gizon, L., & Sreenivasan, K. R. 2016, Ann. Rev. Fluid Mech., 48, 191

Hotta, H., & Kusano, K. 2021, Nat. Astron., 5, 1100

Hotta, H., Rempel, M., & Yokoyama, T. 2015, ApJ, 798, 51

Hotta, H., Rempel, M., & Yokoyama, T. 2016, Science, 351, 1427

Hotta, H., Kusano, K., & Shimada, R. 2022, ApJ, 933, 199

Käpylä, P. J. 2019a, A&A, 622, A195

Käpylä, P. J. 2019b, A&A, 631, A122

Käpylä, P. J. 2021, A&A, 655, A78

Käpylä, P. J. 2022, ApJ, 931, L17

Käpylä, P. J., Mantere, M. J., Cole, E., Warnecke, J., & Brandenburg, A. 2013, ApJ, 778, 41

Käpylä, P. J., Käpylä, M. J., & Brandenburg, A. 2014, A&A, 570, A43

Käpylä, P. J., Käpylä, M. J., Olspert, N., Warnecke, J., & Brandenburg, A. 2017, A&A, 599, A4

Käpylä, P. J., Viviani, M., Käpylä, M. J., Brandenburg, A., & Spada, F. 2019, Geophys. Astrophys. Fluid Dyn., 113, 149

Käpylä, P. J., Gent, F. A., Olspert, N., Käpylä, M. J., & Brandenburg, A. 2020, Geophys. Astrophys. Fluid Dyn., 114, 8

Karak, B. B., Käpylä, P. J., Käpylä, M. J., et al. 2015, A&A, 576, A26

Karak, B. B., Miesch, M., & Bekki, Y. 2018, Phys. Fluids, 30, 046602

Kitchatinov, L. L., & Rüdiger, G. 2004, Astron. Nachr., 325, 496

Kitchatinov, L. L., & Rüdiger, G. 2005, Astron. Nachr., 326, 379

Kupka, F., & Muthsam, H. J. 2017, Liv. Rev. Comp. Astrophys., 3, 1

Matilsky, L. I., Hindman, B. W., & Toomre, J. 2020, ApJ, 898, 111

Miesch, M. S., & Toomre, J. 2009, Ann. Rev. Fluid Mech., 41, 317

Mitra, D., Tavakol, R., Brandenburg, A., & Moss, D. 2009, ApJ, 697, 923

O'Mara, B., Miesch, M. S., Featherstone, N. A., & Augustson, K. C. 2016, AdSpR, 58, 1475

Ossendrijver, M. 2003, A&ARv, 11, 287

Brandenburg, A. 2021, J. Open Source Softw., 6, 2807

Rogachevskii, I., & Kleeorin, N. 2015, J. Plasma Phys., 81, 395810504

Rüdiger, G. 1989, Differential Rotation and Stellar Convection. Sun and Solar-type Stars (Berlin: Akademie Verlag)

Rüdiger, G., & Hollerbach, R. 2004, The Magnetic Universe: Geophysical and Astrophysical Dynamo Theory (Weinheim: Wiley-VCH)

Rüdiger, G., Küker, M., Käpylä, P. J., & Strassmeier, K. G. 2019, A&A, 630, A109

Schrinner, M., Petitdemange, L., & Dormy, E. 2012, ApJ, 752, 121

Schumacher, J., & Sreenivasan, K. R. 2020, Rev. Mod. Phys., 92, 041001

Simitev, R. D., Kosovichev, A. G., & Busse, F. H. 2015, ApJ, 810, 80

Viviani, M., Warnecke, J., Käpylä, M. J., et al. 2018, A&A, 616, A160

Weiss, A., Hillebrandt, W., Thomas, H.-C., & Ritter, H. 2004, Cox and Giuli's Principles of Stellar Structure (Cambridge: Cambridge Scientific Publishers Ltd)